Electronic Supplementary Material (ESI) for Environmental Science: Nano.
This journal is © The Royal Society of Chemistry 2020

Rh-doped $SrTiO_3$ inverse opal with piezoelectric effect for enhanced visible-light-driven photodegradation of bisphenol A

Qian Zhou [a], Qingyun Shi [a], Najun Li*, [a, b], Dongyun Chen [a, b], Qingfeng Xu [a, b], Hua Li [a, b], Jinghui He [a, b], Jianmei Lu*, [a, b]

[a] *College of Chemistry, Chemical Engineering and Materials Science, Collaborative Innovation Center of Suzhou Nano Science and Technology, Soochow University, Suzhou 215123, China*

[b] *National Center of International Research on Intelligent New Nanomaterials and Detection Technologies in Environmental Protection, Suzhou 215123, China*

**Correspondence to: J. M. Lu (E-mail: lujm@suda.edu.cn) & N. J. Li (E-mail: linajun@suda.edu.cn), Tel.: 86 512 65880368*

Supporting Information

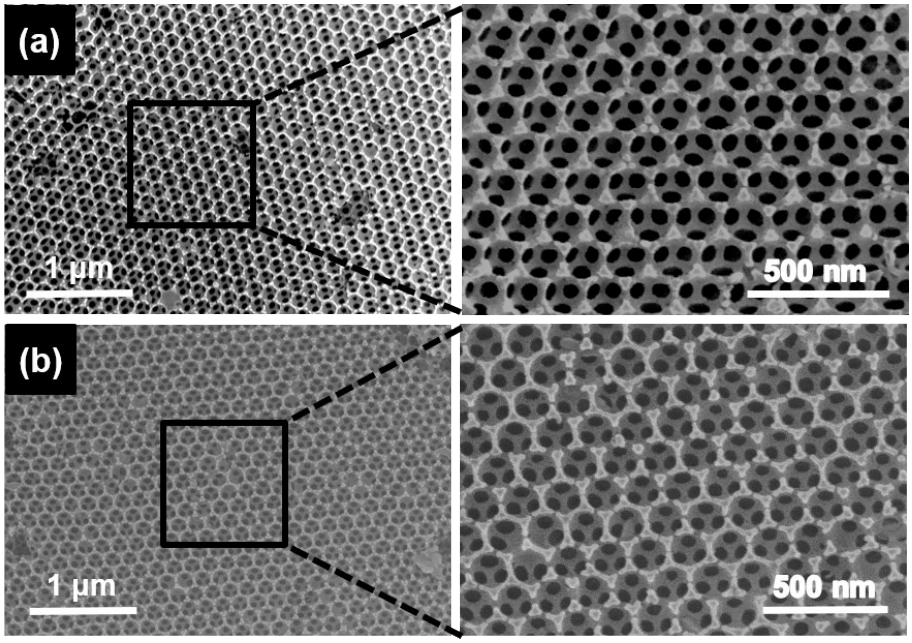

Fig. S1 SEM image of (a) 0.3% Rh-STO IO and (b) 1.0% Rh-STO IO

Calculation of photonic crystal stop-band position

The stop-band of the inverse opal is estimated according to the modified Bragg's law as shown in Equation 1:

$$\lambda max = 2\sqrt{\frac{2}{3}}D\sqrt{n_{eff}^2 - sin^2\theta} = 1.633D\sqrt{f \cdot n_{SrTiO3}^2 + n_{air}^2(1-f)} \quad (1)$$

Where λ_{max} is the biggest wavelength of the reflection peak position (the position of photonic stop-band), D is the diameter of STO IO, n_{SrTiO3} and n_{void} are the refractive index of $SrTiO_3$(2.409) and air, respectively, f is the phase volume percentage of $SrTiO_3$, generally 0.26, and θ is the incidence angle of incident light. For normal incidence, θ = 0. Therefore, according to equation (1) and taking into account the shrinkage of the pore size of the inverse opal during the removal of the PS template, the resulting stop-band of the STO IO is about 380 nm. From the UV-vis absorption spectra, the intrinsic absorption band of STO IO is around 380 nm. According to the slow photon effect, when energy of the slow photon at the edge of the photonic bandgap overlaps with the electron absorption band of the semiconductor, the photocatalyst will have a stronger absorption towards light. Therefore, 280 nm PS microspheres were selected as an opal template for the preparation of STO IO.

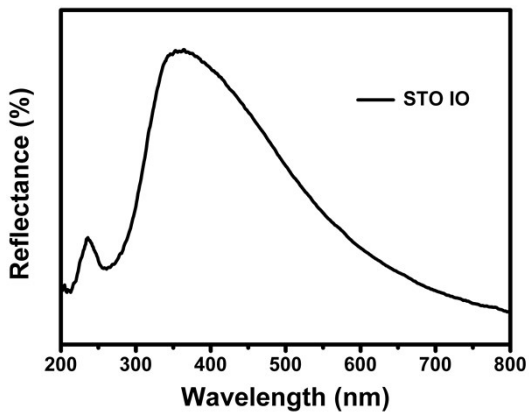

Fig. S2 UV-vis reflectance spectra of STO IO

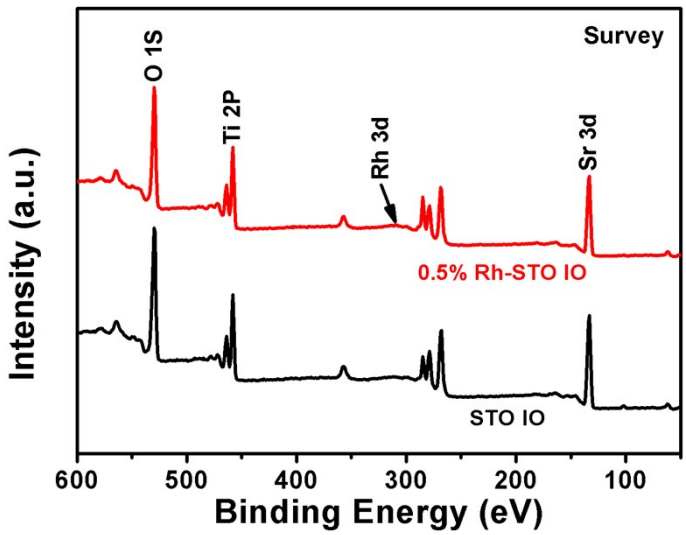

Fig. S3 The survey spectrum of STO IO and 0.5% Rh-STO IO

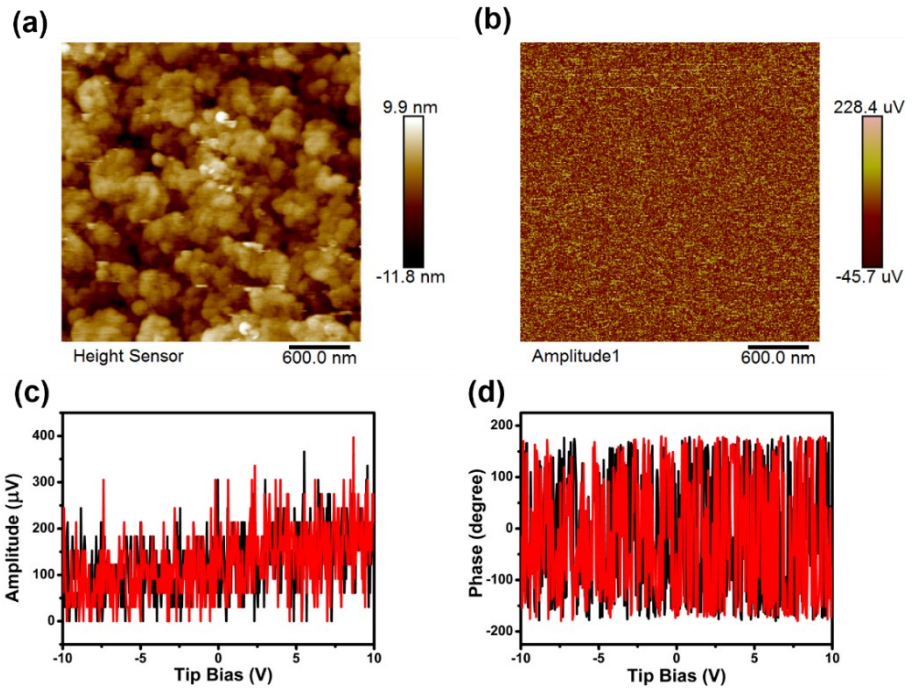

Fig. S4 (a) topography PFM image, (b) amplitude responsive image of piezoelectric potential output and (c, d) amplitude/phase-voltage loop of P25.

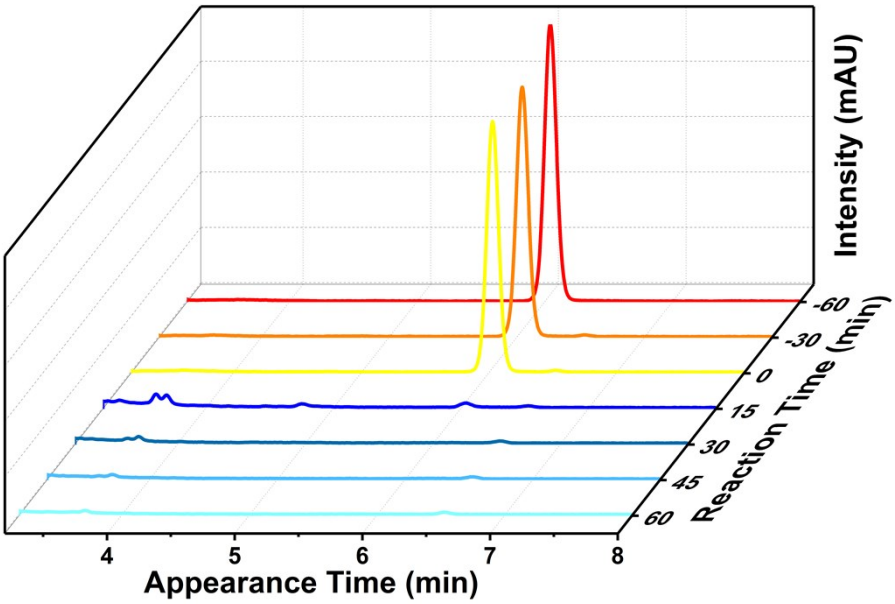

Fig. S5 HPLC diagram of piezoelectric photocatalytic BPA degradation by 0.5% Rh-STO IO

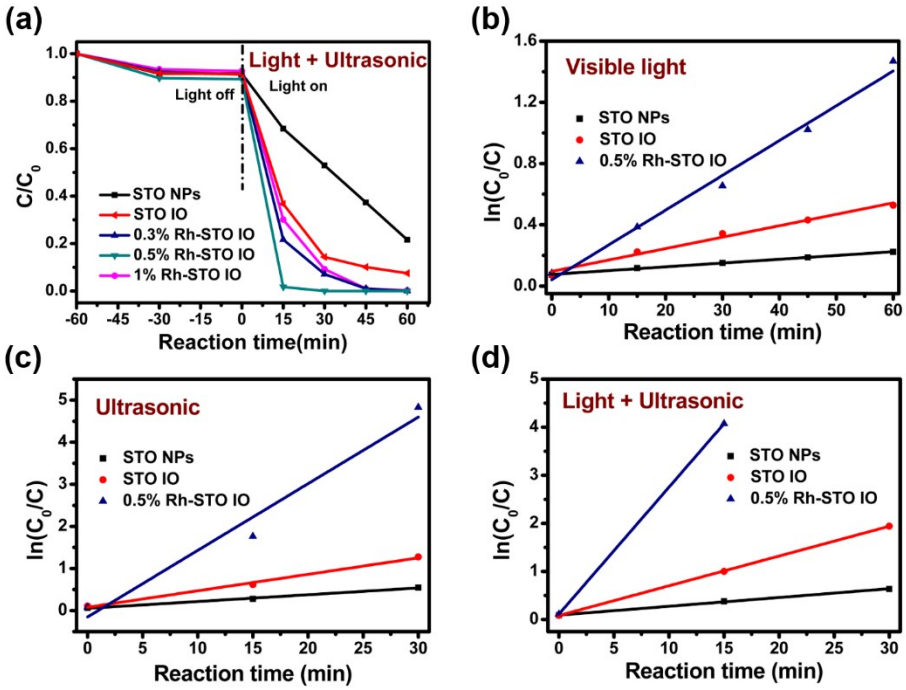

Fig. S6 (a) BPA degradation curves of all samples under ultrasound-assisted visible light catalysis. Pseudo-first-order kinetic fitting curves of STO NPs, STO IO, and 0.5% Rh-STO IO under different catalytic conditions: (b) visible light irradiation, (c) ultrasonic vibration and (d) ultrasonic-assisted visible light irradiation.

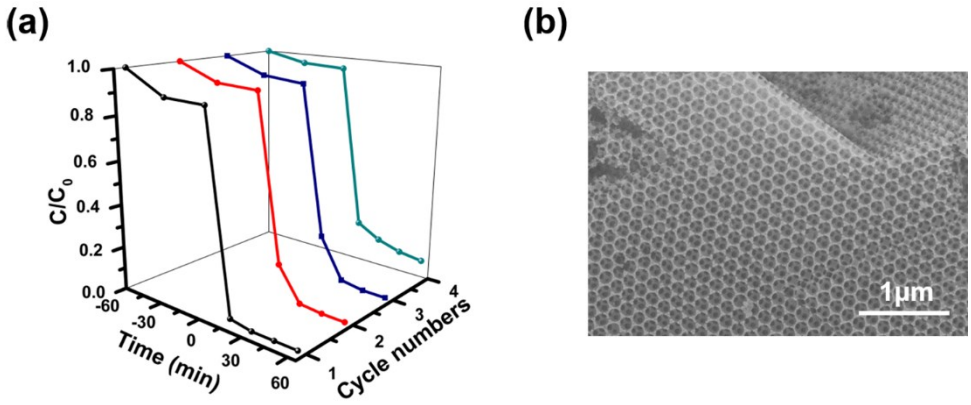

Fig. S7 (a) Cycling performance of piezo-photocatalytic BPA degradation over 0.5% Rh-STO IO and (b) SEM image of 0.5% Rh-STO IO after cycling test.

Stability of the piezo-photocatalytic activity is also significant to practical application of piezo-photocatalyst. The 0.5% Rh-STO IO sample is selected for conducting piezo-photocatalytic cycling tests. As shown in **Fig. S7**(a), the catalyst exhibits similar BPA degradation efficiency in four cycles. The SEM image of 0.5% Rh-STO IO after cycling is depicted in **Fig. S7**(b). The Rh-STO IO still maintains a three-dimensional skeleton structure. The above studies show that Rh-STO IO has good stability under the condition of ultrasonic-assisted visible light irradiation.

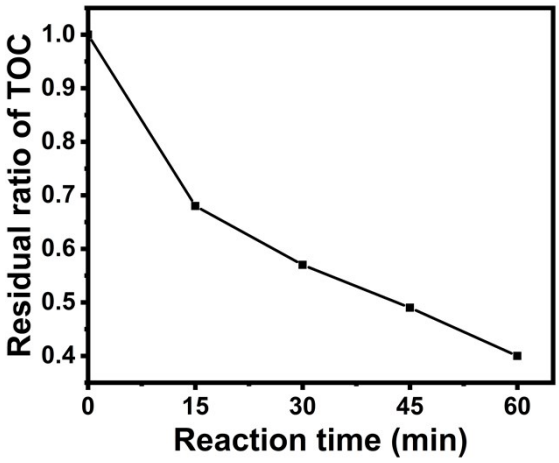

Fig. S8 Removal of TOC by 0.5% Rh-STO IO during the piezo-photocatalytic degradation of BPA.

Total organic carbon (TOC) analysis was carried out to assess the mineralization of BPA (**Fig. S8**). After 60-min visible light irradiation, 60% of the TOC in the reaction system was removed, which indicated that 0.5% Rh-STO IO was effective in mineralizing BPA into CO_2 and H_2O, and was expected to achieve complete mineralization.

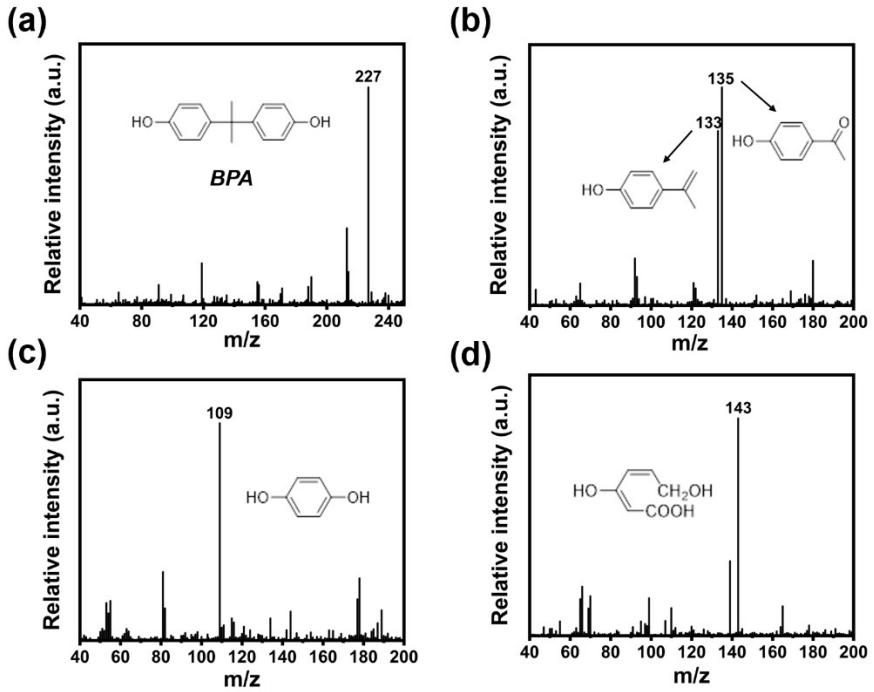

Fig. S9 LC-MS spectra of BPA solution during piezo-photodegradation process by 0.5% Rh-STO IO.

The intermediates generated during the piezo-photodegradation process were analyzed by LC-MS. As shown in **Fig. S9**, BPA and four intermediates were identified. The ion at m/z 227 represents the deprotonated molecule [(M – H)] of BPA (**Fig. S9**a). Two main product ions at m/z 133 and 135 were identified as 4-isopropylphenol and p-hydroxyacetophenone (**Fig. S9**b). Subsequently, the intermediates were further oxidized by the reactive species and transformed into hydroquinone (m/z 109) (**Fig. S9**c). Then, the hydroquinone was oxidized by the direct cleaving of aromatic rings and converted into the intermediate of m/z 143 (**Fig. S9**d). After sufficient reaction time, the degraded products reacted with the active species and were finally mineralized into CO_2 and H_2O.

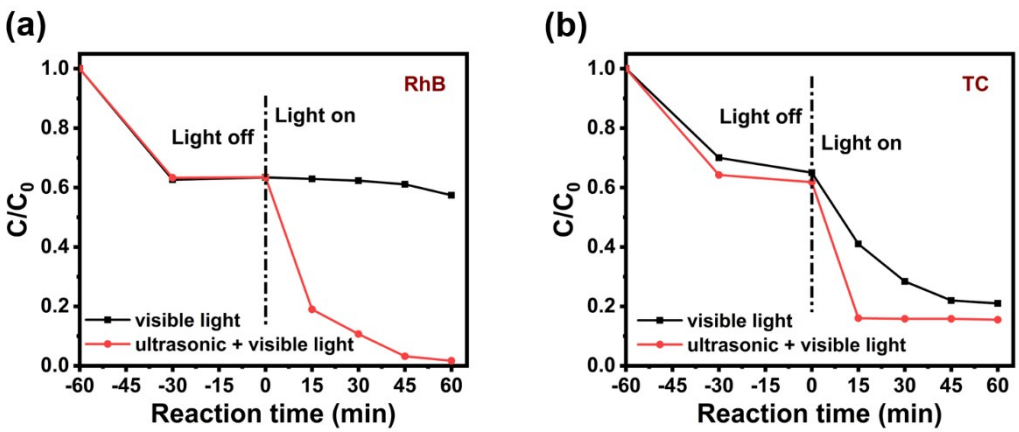

Fig. S10(a) RhB and (b) TC degradation efficiencies of 0.5% Rh-STO IO under different catalytic conditions.

The piezo-photocatalytic activity of the as-prepared sample was further evaluated by the degradation of RhB and TC as model pollutants under different reaction conditions. As depicted in **Fig. S10**, the $SrTiO_3$-based piezo-photocatalytic material has also the efficient degradation efficiency of other environmental pollutants, such as the dye and antibiotic.

Table S1 Comparison of different contaminants photodegradation time and efficiency for the Rh-doped $SrTiO_3$ IO piezo-photocatalyst with reported $SrTiO_3$-based photocatalysts.

Catalyst	Catalyst dosage ($g \cdot L^{-1}$)	Type of pollutant	Initial concentration ($mg \cdot L^{-1}$)	Reaction time (min)	Removal efficiency (%)	Ref.
N-doped $SrTiO_3$	1	MO	5	120	98	[1]
Cr-doped $SrTiO_3$	1	AO7	10	240	95	[2]
V-doped $SrTiO_3$	0.5	MB	10	120	83	[3]
graphene-$SrTiO_3$	0.25	MB	10	120	92	[4]
$MoS_2/SrTiO_3$	1.2	MO	30	60	99.81	[5]
$SrTiO_3$-Ag/AgCl	1	phenol	10	56	72.85	[6]
$SrTiO_3$(La,Cr)/WO_3	0.3	MB	15	120	55	[7]
$SrTiO_3$/BiOI	1	BPA	10	90	90	[8]
Rh-doped $SrTiO_3$ (piezo-photocatalytic)	**0.6**	**BPA**	**10**	**15**	**98.3**	**This work**

References

1. J. Xu, Y. Wei, Y. Huang, J. Wang, X. Zheng, Z. Sun, L. Fan and J. Wu, Solvothermal synthesis nitrogen doped $SrTiO_3$ with high visible light photocatalytic activity, *Ceram. Int.*, 2014, **40**, 10583-10591.
2. D. Hou, X. Hu, W. Ho, P. Hu and Y. Huang, Facile fabrication of porous Cr-doped $SrTiO_3$ nanotubes by electrospinning and their enhanced visible-light-driven photocatalytic properties, *J. Mater. Chem. A*, 2015, **3**, 3935-3943.
3. H. Bantawal, U. S. Shenoy and D. K. Bhat, Vanadium-Doped $SrTiO_3$ Nanocubes: Insight into role of vanadium in improving the photocatalytic activity, *Appl. Surf. Sci.*, 2020, **513**, 145858.
4. H. Bantawal, M. Sethi, U. S. Shenoy and D. K. Bhat, Porous Graphene Wrapped $SrTiO_3$ Nanocomposite: Sr–C Bond as an Effective Coadjutant for High Performance Photocatalytic Degradation of Methylene Blue, *ACS Appl. Nano Mater.*, 2019, **2**, 6629-6636.
5. J. Liu, L. Zhang, N. Li, Q. Tian, J. Zhou and Y. Sun, Synthesis of $MoS_2/SrTiO_3$ composite materials for enhanced photocatalytic activity under UV irradiation, *J. Mater. Chem. A*, 2015, **3**, 706-712.
6. H. Shen, H. Wei, Z. Pan, Y. Lu and Y. Wang, Preparation and characterization of $SrTiO_3$-Ag/AgCl hybrid composite with promoted plasmonic visible light excited photocatalysis, *Appl. Surf. Sci.*, 2017, **423**, 403-416.
7. X. Liu, J. Jiang, Y. Jia, J. Qiu, T. Xia, Y. Zhang, Y. Li and X. Chen, Insight into synergistically enhanced adsorption and visible light photocatalytic performance of Z-scheme heterojunction of $SrTiO_3$(La,Cr)-decorated WO_3 nanosheets, *Appl. Surf. Sci.*, 2017, **412**, 279-289.
8. X.-J. Wen, C.-G. Niu, L. Zhang, C. Liang and G.-M. Zeng, An in depth mechanism insight of the degradation of multiple refractory pollutants via a novel $SrTiO_3$/BiOI heterojunction photocatalysts, *J. Catal.*, 2017, **356**, 283-299.